Magnetic Equivalent Circuit Model for a Two Degree-of-Freedom Rotary-Linear Machine with Transverse Flux Structure

Yaojie He, *Student Member, IEEE*, Guanghui Yang, *Student Member, IEEE*, Shuangchun Xie, *Student Member, IEEE*, Fawen Shen, *Student Member, IEEE*, Yuming Yan, *Student Member, IEEE*, and Christopher H. T. Lee, *Senior Member, IEEE*

***Abstract*—This paper proposes a magnetic equivalent circuit (MEC) model for a two degree-of-freedom rotary-linear machine with transverse flux structure. The permeance grid is formed according to the flux pattern generated by finite-element method (FEM). By tuning the leakage flux permeance, the electromagnetic performance of the rotary-linear machine calculated by the MEC model shows good alignment to that by FEM. To fully demonstrate the benefits of the MEC model, the calculation accuracy and time consumption comparisons among the MEC model, magnetomotive force (MMF) model, and FEM are conducted. In addition, the MEC model is applied to the parametric study, which proves that the MEC model is capable of obtaining the accurate results under various geometry designs. Based on that, a hierarchy optimization flow is put forward which is a practical method for global optimization on 3D structure. Finally, an experimental prototype is manufactured to verify the proposed concepts.**

***Index Terms*—Magnetic equivalent circuit model, rotary-linear machines, two degree-of-freedom machine, 3-D finite-element method.**

I. INTRODUCTION

TWO degree-of-freedom (2DOF) rotary-linear (RL) electric machines have been extensively investigated due to numerous benefits [1]-[3]. Compared with the conventional dual-machine RL system, 2DOF RL electric machines offer higher robustness, greater space utilization, and less necessary mechanical adjustment. One group of 2DOF RL electric machines are termed as coupled-flux RL machines, where the magnetic fields of rotary and linear motions are combined in one space [4]. Thus, the working fluxes of two motions are physically coupled, and the 2DOF control can be achieved by winding configuration or decoupling algorithm [5]-[8]. This unique feature allows coupled-flux RL machines to employ the merits as high level of integration, high dynamic performance, and high material utilization rate, which make coupled-flux RL machines promising candidates for those applications requiring multi-direction movements and sensitive to machine volume (e.g., pick & place robot arm, tunning machine, electromagnetic suspension device and energy harvest system). Particularly, in electric vehicles, coupled-flux RL machines are able to integrate with the in-wheel electric motors to accomplish driving, steering, and suspension by each wheel individually. Also, the vibration and noise can be significantly mitigated due to the lack of solid connection mechanisms.

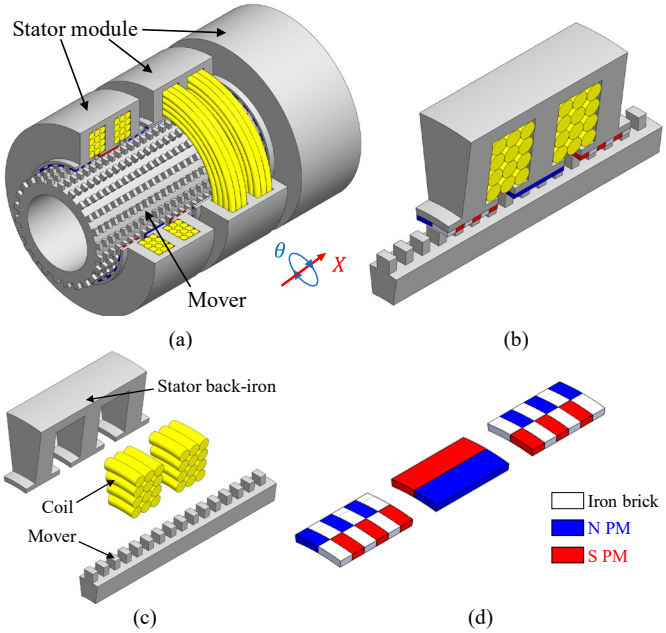

Fig. 1. Topology of the TF-RL machine. (a) Assembled structure. (b) Partial structure. (c) Stator back-iron, toroidal coils, and mover in partial structure. (d) PMs array.

One of the most advanced coupled-flux RL machines is the modular transverse-flux RL (TF-RL) machine [9], which exhibits the advantages as high linear force, high rotary torque machine is depicted in Fig. 1. The mover exhibits mechanical saliency along both circumferential and axial directions. The stator module features two toroidal coils embedded in an E-shape back iron. A radially magnetized PMs array is mounted on the inner surfaces of three stator poles, whose arrangement is illustrated in Fig. 1(d). Due to the unique PMs array, the pole-pair numbers of the working fluxes of rotary and linear motions are different. By applying specially edited current profiles, the rotary and linear motions can be controlled individually.

Despite the benefits, one of the major challenges facing the TF-RL machine is that the design and optimization processes are very time consuming by Finite Element Method (FEM). This is due in part of the complex PMs array and structure, which necessitates numerous attempts and tests under three-dimensional (3D) model to verify the working principle. Additionally, the number of geometry parameters in coupled-flux RL machines are significantly larger than those in

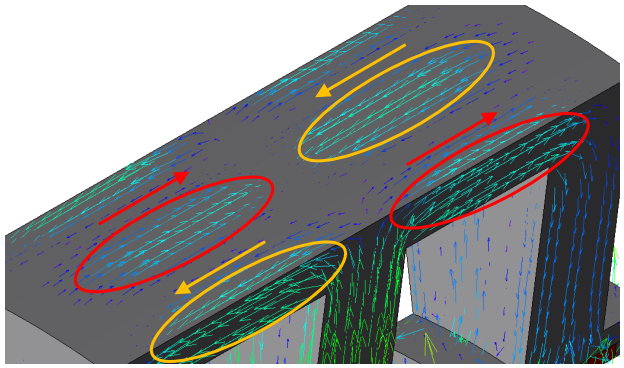

(a)

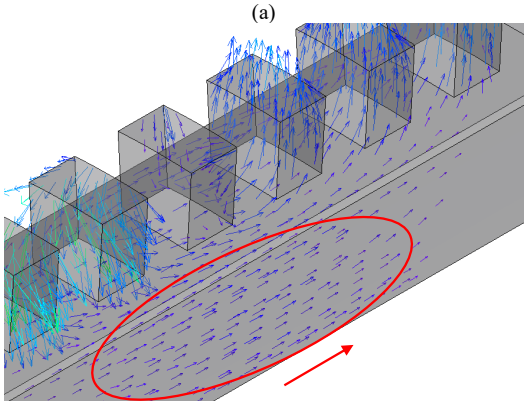

(b)

Fig. 2. Flux pattern by FEM. (a) Stator module. (b) Mover.

conventional rotary or linear machine, making the optimization process even more difficult. As the result, the method with fast performance and competitive accuracy is necessitated in obtaining the optimal design of the TF-RL machine.

The analytical model has been widely studied in literatures [10]-[15] for shortening the time consumption on simulation and optimization on electric machines. Among them the magnetic equivalent circuit (MEC) model which has been proven to be a promising option for performance calculation. Compared with the magnetomotive force (MMF) model, which requires the determination of airgap MMF and permeance distribution, the MEC model can provide more accurate results since it takes account of practical permeability, saturation effect, as well as the leakage flux. Moreover, the MMF model only evaluates a limited number of geometry parameters, so it is not suitable for the global geometry optimization. In contrast, the MEC model is capable of quantifying the effect of each geometry parameter on the output performance. Especially, the MEC model is favored by those electric machines with 3D flux path, since it can significantly shrink the simulation time to seconds, compared with hours of FEM simulation.

Particularly, the 3D MEC models for transverse structure in 1DOF electric machines have been widely investigated [16]-[19]. Notably, since only one motion is conducted in those TF machines, the airgap permeance variation is estimated based on a simple planar pattern. However, in TF-RL machines, the magnetic field of two motions are merged, resulting that the airgap permeance is affected by both rotary and linear motions. It means the airgap flux path will be twisted into a solid entity, and the conventional 2D pattern is no longer applicable. Hence, for accurately reflecting the airgap flux path and permeance variation, a complex 3D flux pattern is necessitated. In addition, the airgap flux in TF-RL machines transforms along rotary and linear motions synchronously rather than combining separated variations in each motion. Consequently, the conventional MEC models are not suitable to be used in 2DOF machines.

In recent years, the employment of MEC model in 2DOF machines has been investigated [20]. In that paper, the leakage flux is accurately estimated by integrating the analytical Laplace equation and MEC network. However, the magnetic potential drop in the iron part is missed. As a result, not only the magnetic field generated by the armature current is not discussed, but the geometry of the iron parts cannot be optimized. While it offers competitive precision on the no-load performance calculation (i.e., back-EMFs, cogging torque and detent force), the lack of on-load performance and parametric studies limits its utilization in the global geometry optimization.

In this paper, a 3D MEC model is proposed for calculating the electromagnetic performance of a TF-RL machine. The detailed procedures of the permeance grid formation and permeance calculation will be presented in the subsequent sections. By adopting a full-scale permeance network, the magnetic distribution in every segment of the studied machine can be illustrated. Besides, the airgap permeance is divided into several 3D solid components. Hence, the airgap permeance variation can be explored comprehensively and accurately. To evaluate the attractiveness of the proposed MEC model, a comparison regarding the accuracy and time consumption is conducted with MMF model and FEM. Finally, the effectiveness of the MEC model under various geometry designs is verified, and the optimization chart is put forward.

II. Model Formation

A. Permeance Grid

The flux path pattern of TF-RL machine by FEM is shown in Fig. 2. Since the PMs are alternating along the circumferential direction, two parallel flux paths with opposite axial directions are formed in the stator yoke part between two stator poles. Likewise, two flux paths with opposite axial directions are illustrated upon the same circumferential position. Nonetheless, the flux flows unidirectionally in the mover side. Hence, a dual-loop grid ought to be formed for the flux in the stator while a single-loop grid is applied in the mover side.

The diagram of the permeance formation in the MEC model is presented in Fig. 3(a). Specifically, only one flux path exists in the stator pole and yoke. Thus, the back-iron of stator module can be integrated as two series connected permeances. Similarly, in the mover side, the mover tooth and mover yoke can be converted to two isolated permeances.

Nonetheless, the flux pattern in the stator shoe and PMs array is much more complex than that in the aforementioned parts. The permeance pattern of the PMs, iron bricks and iron shoe are obtained based on the flux pattern by FEM, which is shown in Fig. 3(b). Those permeances stand for PMs and iron bricks are entitled with the subscripts of “pm” and “ir”, respectively.

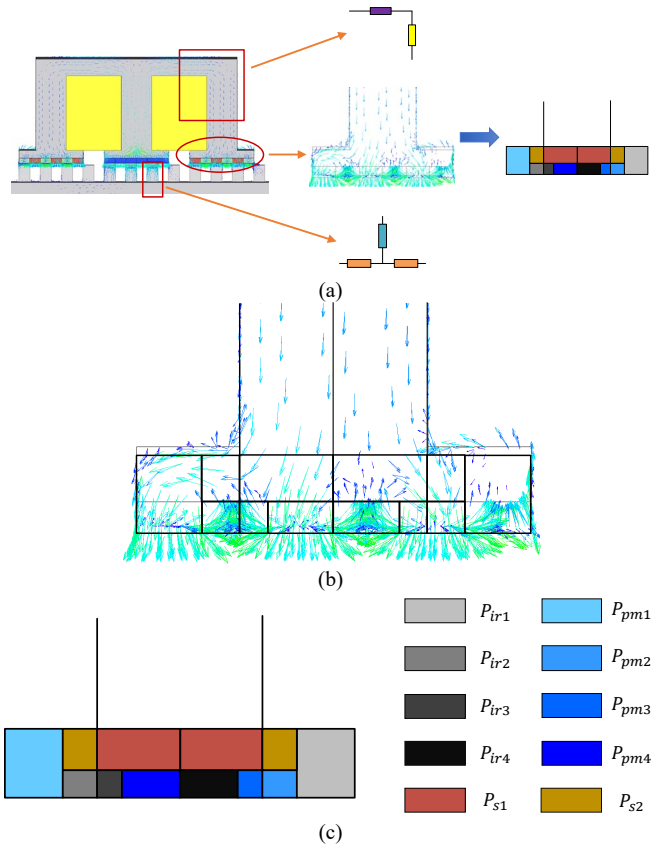

Fig. 3. Flux pattern and permeance model in stator pole. (a) Permeance formation diagram. (b) Flux pattern in stator pole, stator shoe, and PMs array by FEM. (c) Permeances allocation.

Additionally, the numbers in the subscripts of those permeance are arranged by the sequence of their location from outside to inside of the stator pole. Particularly, at two axial terminals of the stator pole, the PMs brick or iron brick is merged with the corresponding part of the stator shoe. P_{s1} and P_{s2} represent the permeances which transmit the flux from PMs array to the stator pole. It should be mentioned that the number of the PMs array permeances is varied with its axial pole-pair number, and the flux path in each permeance aligns with that in FEM results.

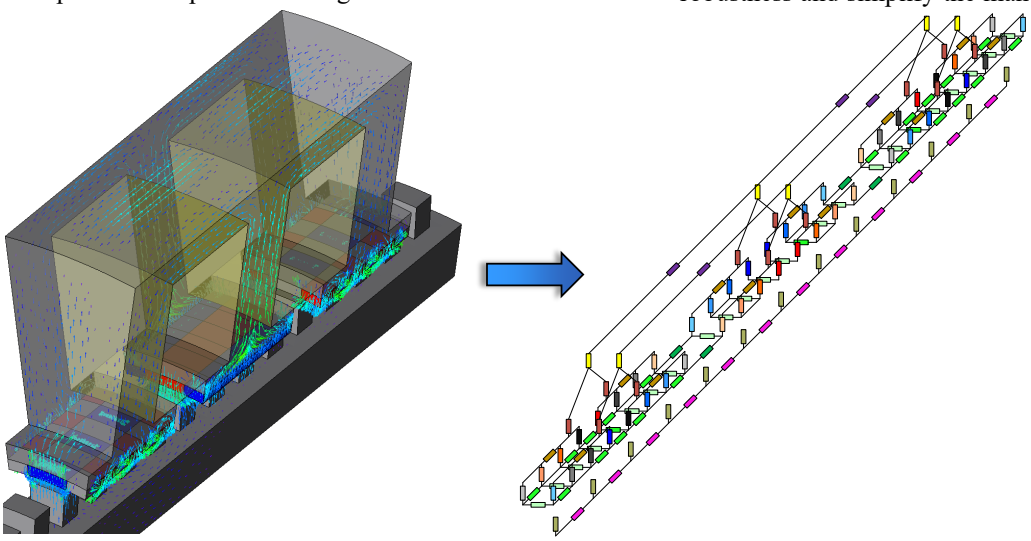

Fig. 5. Permeance grid of partial model with leakage flux path.

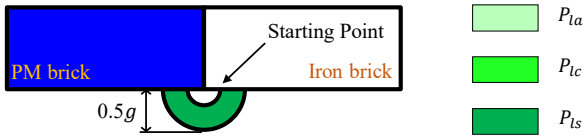

Fig. 4. Leakage flux path and permeance categories.

B. Leakage flux permeance

The power factor issue poses a big challenge in TF-RL machine, with one of major factors as the leakage flux generated by the PMs array. Neglecting the effect of leakage flux (e.g., MMF model) leads to inaccuracy in performance calculation. As illustrated in Fig. 4, P_{la} and P_{lc} represent the leakage flux permeance in axial and circumferential directions, respectively. P_{ls} means the flux leakage between two stator poles. These three permeances can be calculated as:

$$P_{la} = \int_{\alpha l_{pm}}^{0.5g} \frac{\mu_0 R_{si}}{p_r x} dx = \frac{\mu_0 R_{si}}{p_r} \ln\left(\frac{g}{2\alpha l_{pm}}\right) \quad (1)$$

$$P_{lc} = 2\int_{\beta\frac{\pi R_{si}}{p_r}}^{0.5g} \frac{l_{pm}}{\pi x} dx = \frac{2\mu_0 l_{pm}}{\pi} \ln\left(\frac{g p_r}{2\beta\pi R_{si}}\right) \quad (2)$$

$$P_{ls} = \mu_0 \frac{\pi\left[\left(R_{si}+h_{pm}\right)^2 - R_{si}^2\right]}{4 p_r l_{pm}} \quad (3)$$

where

- g is the airgap radial height.
- l_{pm} is the PM brick axial length.
- R_{si} is the stator pole inner radius.
- p_r is the pole-pair number of PMs array in circumferential direction.
- h_{pm} is the PM brick radial height.

α and β are denoted as the starting points of leakage flux in axial and circumferential directions, respectively.

Unlike conventional rotary and linear machines, the PM and iron bricks in the TF-RL machine are designed to be full pitched in both axial and circumferential directions to enhance robustness and simplify the manufacturing process. Therefore,

the starting point of the leakage flux path is a crucial variable in determining the accuracy of the MEC model. Hence, α and β should be tuned to align the simulation results by FEM. The whole permeance grid is presented in Fig. 5.

C. Airgap permeance

The airgap permeance is the essential part in MEC models. The qualitative characteristic and quantitative performance of the TF-RL machine depend on the evaluation on the airgap permeance variation. In Fig. 6, a basic airgap permeance diagram varying with linear motion in 2D pattern is illustrated, where l_{mt} is the axial length of mover tooth.

Those flux path are deduced based on the assumptions as:

- Flux flows radial in middle of airgap region.
- Flux flows in a quarter of circle among the mover yoke and iron brick side surface.
- No flux flows to the side surface PM brick.

It should be mentioned the flux path patterns could be different when some geometry parameters are changed (e.g., $l_{pm}<l_{mt}$). In such case, the diagram in Fig. 6 should be modified. Similarly, a similar airgap permeance variation diagram can be deduced under rotary motion as well.

For accurately depicting the magnetic field in the airgap, a 3D airgap permeance pattern is formed and illustrated in Fig. 7. The front surface means the surface adjacent to the airgap with the normal vector pointing at the radial direction, while the side surface exhibits the normal vector pointing at the axial direction. It is noted that the green and blue parts are particularly set for calculating the longitude end effect as it represents the flux flowing through the side surface of the iron brick, which locate out of the stator module.

In conventional rotary or linear machines, the thickness of the airgap permeance is constant, which is same as the lamination thickness. Nonetheless, in the 3D model, the airgap permeance is determined by both axial and circumferential position of the mover. Hence, the thickness of the airgap permeance is a dynamic variable. For instance, when evaluating the airgap permeance variation under linear motion, the thickness of the airgap permeance in circumferential direction should be calculated based on the overlapped width of the PMs array brick and the mover tooth along circumferential direction. Another distinguished feature in 3D the airgap permeance pattern is that the flux from the side surface of the iron brick to that of the mover tooth, which is not shown under 2D pattern, should be accounted. This kind of permeance is applied to those iron bricks located at the axial end of the stator module.

III. Performance Comparison

In this section, the leakage flux tuning process is conducted for fitting the results calculated by the MEC model to that by FEM. After that, the coil-flux linkages, coil back electromagnetic forces (back-EMFs), linear force and rotary torque generated by the MEC and MMF models are compared to those by FEM. The major parameters of the TF-RL machine are presented in Table I. To ensure a three-phase system for linear motions, the axial gap between two adjacent stator modules follows the condition:

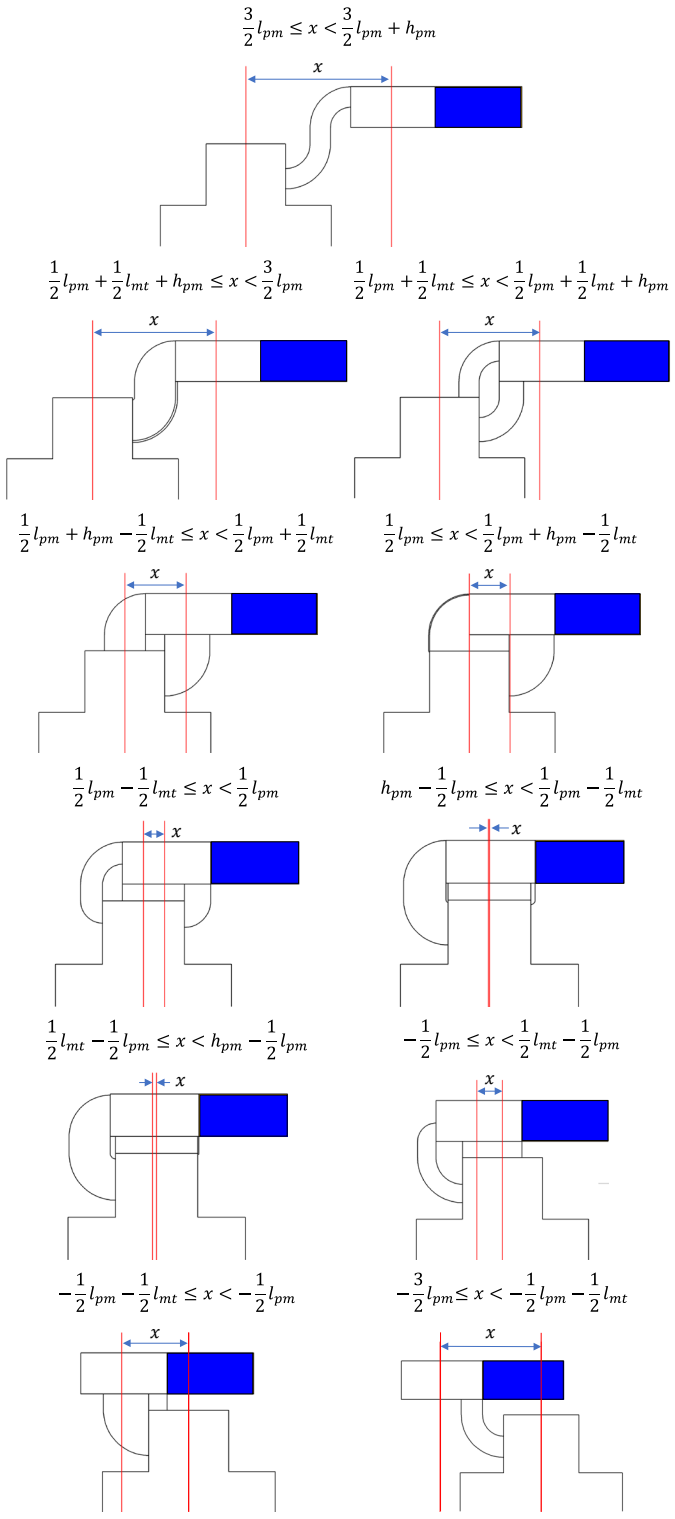

Fig. 6. Basic airgap permeance variation under linear motion.

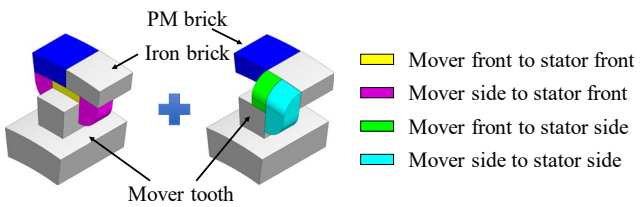

Fig. 7. Airgap flux path and permeance pattern.

TABLE I
MAJOR PARAMETERS OF THE COUPLED-FLUX RL MACHINES

Symbol	Description	Original	Optimized
R_{sor}	Stator outer radius (mm)	100	
h_{sy}	Stator yoke height (mm)	3	
l_{sp}	Stator pole length (mm)	24	
h_p	Stator shoe/pole height (mm)	7.5	
p_a	PM axial pole-pair number	4.2	
p_c	PM circumferential pole-pair number	1.2	
w_{pm}	PM pole width arc (deg)	5	6.6
l_{pm}	PM pole length (mm)	10	12
h_{pm}	PM pole height (mm)	2	3
g	Airgap length (mm)	2.5	2
w_{mt}	Mover tooth width arc (deg)	7.5	6.2
l_{mt}	Mover tooth length (mm)	4	4.3
h_{mt}	Mover tooth height (mm)	7.5	8.2
h_{my}	Mover yoke height (mm)	9	11.1
R_{shaft}	Inner shaft radius (mm)	40	
l_d	Axial module gap (mm)	5.6	
l_a	Total axial length (mm)	288.4	
v_l	Rated linear speed (m/s)	0.588	
n_r	Rated rotary speed (rpm)	250	

$$l_{gap} = (n \pm \frac{1}{3})\tau_a \quad (n = 1,2,3...) \tag{4}$$

where τ_a is the axial pole pitch of the PMs array. Similarly, a mechanical shifting is conducted along the circumferential direction for the rotary system. Besides, it is noted that such gap should be sufficient large to guarantee the magnetic isolation.

A. Leakage flux tuning in the MEC model

As mentioned above, since the PM array is full-pitch in both axial and circumferential directions, the starting points for calculating the leakage flux between the adjacent bricks should be initially set. Besides, the starting points directly affects the leakage flux permeance, so as the distribution of the working flux and leakage flux. It implies that the results from the MEC model can be modified by adjusting the starting points to make sure they are close to the counterparts by FEM. As a result, in Fig. 8, the fundamental component of the coil flux linkage under various combinations of α and β are illustrated. The black mesh with yellow dots is the reference value by FEM.

It is evident that the fundamental component of coil flux linkage under linear and rotary motions are mostly affected by α and β, respectively. As a result, the coil flux linkage under two motions by the MEC model can be individually tuned. Another characteristic is that the fundamental component of the coil flux linkage is enlarged when α and β are enhanced. This is because when α and β are increased, the leakage flux path gets narrow, and the average length of the leakage flux path is larger. Thus, the leakage flux permeance becomes smaller, and a larger amount of working flux is obtained. After the tuning process, the values of α and β are fixed, and the MEC model has been formed properly, which is utilized in comparison.

B. No-load performance comparison

In [9], the working fluxes of rotary and linear motions in each coil can be quantitatively calculated by the MMF model, which are expressed as:

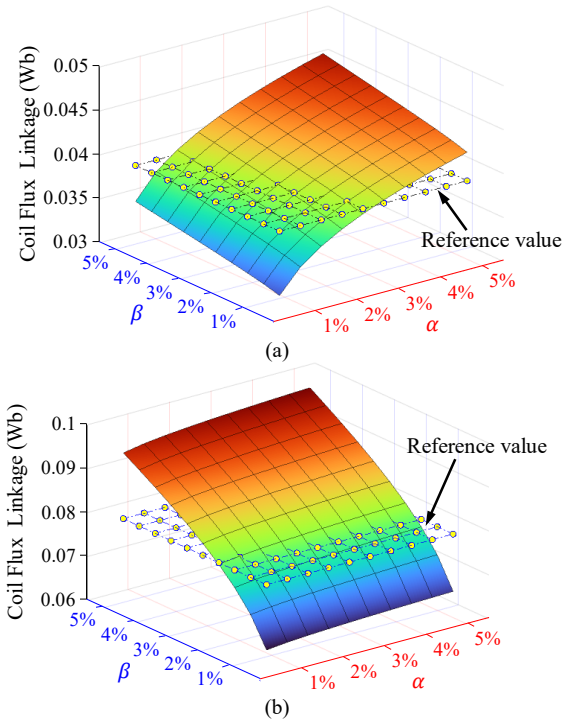

Fig. 8. Fundamental component of coil flux linkage. (a) Linear motion (b) Rotary motion.

$$\phi_R = \sum_{n_F=1}^{\infty} \frac{4pA_{0n_F}P_{00}w_{pm}l_{pm}}{n_F\pi}\cos\left(\frac{2n_F\pi}{3}\right)\sin\left(\frac{n_F\pi p_a}{p}\right) + \sum_{m_F,n_F=1}^{\infty}\left\{\frac{pC_{m_Fn_F}P_{m_F0}w_{pm}l_{pm}}{n_F\pi}\cos\left(\frac{2n_F\pi}{3}\right)\sin\left(\frac{n_F\pi p_a}{p}\right)\sin\left[\frac{m_F\pi(\omega t+\theta_0)}{w_{pm}}\right]\right\} \tag{5}$$

$$\phi_L = \sum_{\substack{n_F=1\\ n_p=1}}^{\infty} 2P_{0n_p}A_{0n_F}w_{pm}\left\{\begin{aligned}&L_1\left(n_p,n_F,\frac{2}{3}p\right)\cos\left[\frac{n_p\pi(vt+x_0)}{l_{pm}}\right]\\ &+L_2\left(n_p,n_F,\frac{2}{3}p\right)\sin\left[\frac{n_p\pi(vt+x_0)}{l_{pm}}\right]\end{aligned}\right\} \tag{6}$$

where

- p_a is the pole-pair number of PMs array in axial direction.
- w_{pm} is the PM brick circumferential width.
- F_{pm} is the airgap MMF of PMs array.
- ω and v are the speeds of rotary and linear motions, respectively.
- θ_0 and x_0 are the initial electric phase angles in the circumferential and axial directions, respectively.
- A_{0n_F}, $C_{m_Fn_F}$, P_{00}, P_{m_F0}, and P_{0n_F} are the coefficients related to the geometry data.

p, L_1 and L_2 are calculated as:

$$p = 3(p_a+1) \tag{7}$$

$$L_1(n_p,n_F,s) = \frac{pl_{pm}}{(n_F-pn_p)\pi}\cos\left[\frac{(n_F-pn_p)\pi s}{p}\right]\sin\left[\frac{(n_F-pn_p)\pi p_a}{p}\right] + \frac{pl_{pm}}{(n_F+pn_p)\pi}\cos\left[\frac{(n_F+pn_p)\pi s}{p}\right]\sin\left[\frac{(n_F+pn_p)\pi p_a}{p}\right] \tag{8}$$

$$L_2\left(n_p,n_F,s\right)=\frac{pl_{pm}}{\left(n_F-pn_p\right)\pi}\sin\left[\frac{\left(n_F-pn_p\right)\pi s}{p}\right]\sin\left[\frac{\left(n_F-pn_p\right)\pi p_a}{p}\right]$$
$$-\frac{pl_{pm}}{\left(n_F+pn_p\right)\pi}\sin\left[\frac{\left(n_F+pn_p\right)\pi s}{p}\right]\sin\left[\frac{\left(n_F+pn_p\right)\pi p_a}{p}\right] \quad (9)$$

The results of the coil flux linkage and back-EMF obtained by MEC, MMF and FEM models are presented in Fig. 9 and Table II. Compared with the results from FEM, the fundamental components of the coil flux linkage under linear and rotary motions by MEC model are differed in 4.1% and 2.3%, respectively. After tuning process, the fundamental components of the coil flux linkage in both rotary and linear motions by MEC model show good agreement to those by FEM.

On the contrary, the fundamental components of the rotary and linear coil flux linkage by MMF model are 8.6% and 20.6% higher than those by FEM, respectively. In addition, the rotary coil flux linkage calculated by the MMF model presents higher low-order harmonics than that by FEM. Consequently, the rotary back-EMF by the MMF model shows trapezoidal waveform. The reason behind this large error is that the MMF model lacks the consideration towards the leakage flux, finite permeability and the saturation effect, as well as the twisted 3D flux path in the airgap region, leading to the incorrect estimation towards the magnetic field distribution in both the iron part and airgap region. In conclusion, the MMF model is only suitable for qualitative analysis while MEC model shows its advantage in calculating the working flux quantitatively.

C. On-load performance verification

While the leakage flux tuning process makes the coil flux linkage by the MEC model fitting to that by FEM, the results of other performances obtained by those three methods should be compared as well to fully test the accuracy of those analytical models. Hence, in Fig. 10, the linear force and rotary torque by MEC, MMF and FEM models are presented and compared. The electromagnetic performance of the TF-RL machine obtained by three models are listed in Table II.

In the on-load condition, the linear force and rotary torque obtained from the analytical models are calculated based on following equations:

$$\begin{cases} t_e=\dfrac{60\sum e_c i_c}{4\pi n_r} \\ f_e=\dfrac{\sum e_c i_c}{2l_v} \end{cases} \quad (10)$$

where e_c and i_c are the transient value of coil back-EMF and current. n_r and l_v are the rotary and linear speeds.

Subject to inaccuracy in no-load study, the difference of the on-load performance between MMF model and FEM is substantial. The errors of linear force and rotary torque by MMF model and FEM are 21.80% and 12.78%, respectively. Due to the significant total harmonic distortion (THD) in rotary back-EMF, the torque ripple obtained by the MMF model is the highest among all three methods.

The differences regarding linear force, rotary torque, and torque ripple by the MEC model and FEM are below than 5%.

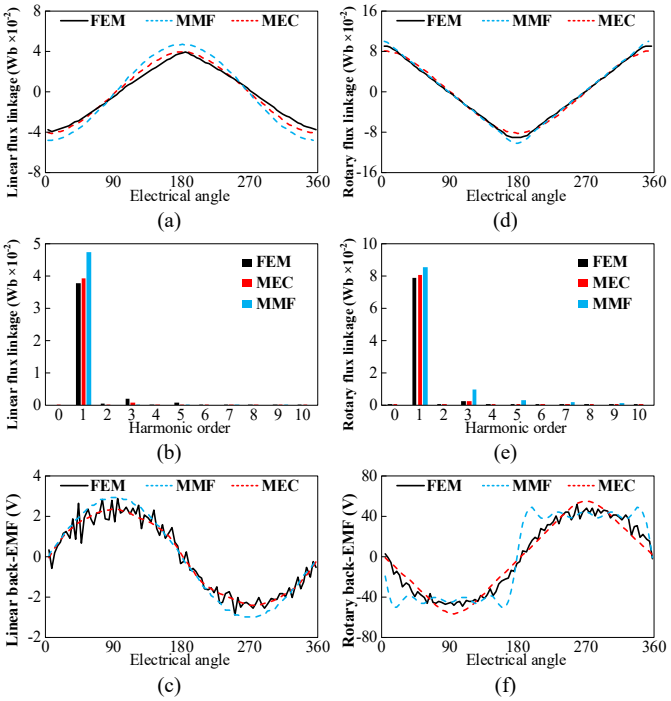

Fig. 9. No-load performance under three models. (a) Linear coil flux linkage. (b) Linear coil flux linkage harmonic spectra. (c) Linear coil back-EMF. (d) Rotary coil flux linkage. (e) Rotary coil flux linkage harmonic spectra. (f) Rotary coil back-EMF.

TABLE II
PERFORMANCE COMPARISON AMONG THREE METHODS

Index	MEC	MMF	FEM
Linear flux linkage amplitude (Wb)	0.040	0.048	0.038
Linear back-EMF amplitude (V)	2.48	3.00	2.46
Linear back-EMF THD	10.65%	0.64%	15.71%
Rotary flux linkage amplitude (Wb)	0.079	0.086	0.081
Rotary back-EMF amplitude (V)	50.85	54.00	49.71
Rotary back-EMF THD	9.57%	42.70%	9.14%
Average linear force (N)	420.15	483.59	397.04
Linear force ripple	11.55%	1.98%	14.35%
Average rotary torque (Nm)	34.46	38.31	33.97
Rotary torque ripple	7.9%	11.39%	8.47%

However, the linear torque ripple obtained by two methods exhibit higher discrepancy. One of the reasons is that leakage flux paths at two axial ends of the stator pole are not evaluated accurately. As a result, the force ripple results from the end-effect cannot be fully reflected in the harmonics of the linear back-EMF. Hence, the force ripple calculated by the MEC model is smaller than that by FEM.

In addition, the results calculated by the MEC model is able to present some qualitative characteristics of the TF-RL machine. In Fig. 11 (a) and (b), the flux linkage waveforms in those two coils in the same stator module under two motions are presented. The linear flux linkages in those two coils are in the same phase, while the rotary flux linkages are complementary with each other. That means, the pole-pair numbers of the linear and rotary fluxes are different. With this unique feature, the linear and rotary motions can be individually controlled by adjusting the electric phase angle of the currents in those two coils, which is basic principle for 2DOF control.

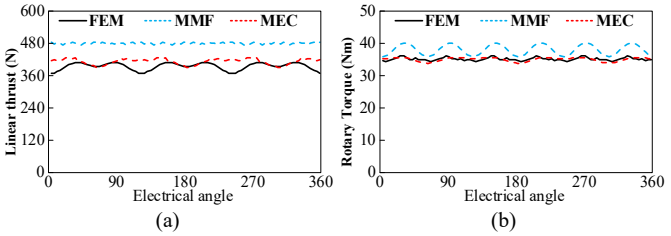

Fig. 10. On-load Performance under three models. (a) Linear force. (b) Rotary torque.

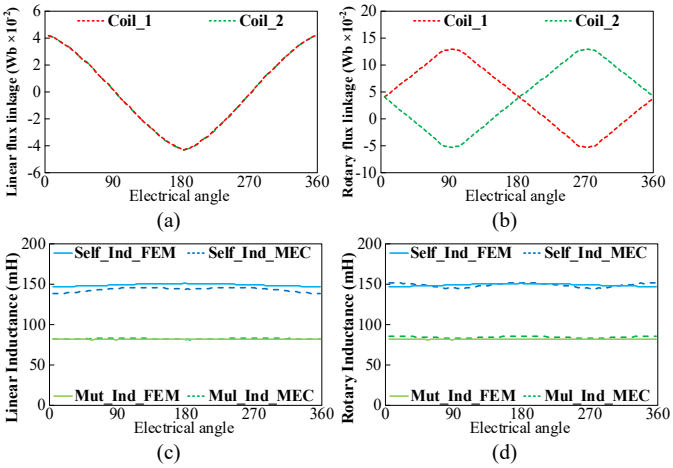

Fig. 11. Flux linkage characteristics in single stator module. (a) Linear motion. (b) Rotary motion. (a) Linear inductance. (b) Rotary inductance.

As mentioned in the former literature, the power factor is one of the most severe issues in TF-RL machines. As a result, the coil inductance should be calculated accurately in the analytical model. Fig. 11(c) and (d) demonstrate the coil inductance under two motions by MEC model and FEM. Due to the modular stator structure, the mutual inductance reflects the magnetic interaction of two coils in the same stator module. It is noted both self-inductance and mutual inductance calculated by the MEC model under two motions demonstrate good alignment with those by FEM, whose differences are below than 5%. It implies that the MEC model holds the potential of precise calculation on the on-load performance of the TF-RL machine.

IV. Parametric Study and Optimization

In the former analysis, the electromagnetic performance of the TF-RL machine calculated by the MEC model shows good agreement to that simulated by FEM. One of the essential arguments is the leakage flux tuning process. However, the α and β are tuned based on one single design with fixed reference value. The effectiveness of the MEC model with fixed α and β for calculating the performance of various geometry designs will be discussed in this section.

A. Parametric study effectiveness

Since the values of α and β directly affect the leakage flux permeance, those geometry parameters which are significantly coherent with the airgap magnetic field should be investigated at first place. Hence, the dimensions of the mover tooth and the

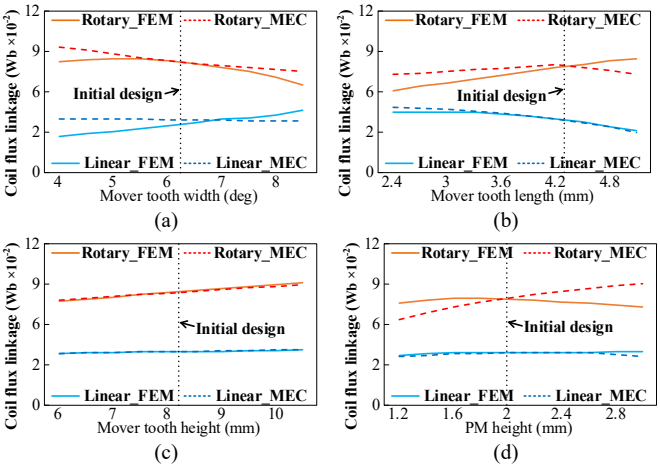

Fig. 12. The amplitude of the fundamental coil flux linkage by MEC model and FEM in parametric studies. (a) Mover tooth circumferential width. (b) Mover tooth axial length. (c) Mover tooth radial height. (d) PM brick radial height.

radial height of PMs array bricks are selected for the parametric studies. Similar to the above analysis, the coil flux linkage is chosen as the objective in the following investigation. The results are shown in Fig. 12.

In the studies of the mover tooth circumferential width, mover tooth axial length, and PM brick radial height, the difference of the results from the MEC model and FEM gets larger when those parameters are far from the initial value. However, such errors are kept almost the same under various mover tooth radial heights. One explanation can be made that once the following condition is fulfilled:

$$h_{mt} \geq l_{pm} - \frac{1}{2} l_{mt} \tag{11}$$

the airgap flux path pattern remains the same. Hence, the ratio of the working flux and leakage flux is constant. Consequently, the fixed α and β are fitted under varied mover tooth heights, and the results from MEC and FEM are very close.

For each parametric study, the largest difference of the coil flux linkage by the MEC model and FEM is below than 20%. With such accuracy, the parameter ranges are close to that in the scope of the optimization towards conventional rotary and linear machines. As a result, the MEC model with constant tuned values of α and β shows competitive accuracy in investigating the optimal performance within a local parameter search space. Thus, an optimization process adopting MEC model can be formed towards the TF-RL machine.

B. Optimization flow

Based on the characteristics of the proposed MEC model, a hierarchical optimization flow chart is hereby composed as presented in Fig. 13. The whole optimization process is divided into three stages, which are named as optimization space formation, MEC model optimization, and verification. It is a hybrid optimization process combining both MEC model and FEM to fulfill high accuracy, as well as high time-efficiency.

The target of the optimization space formation stage is to narrow down the search space for all the geometry parameters.

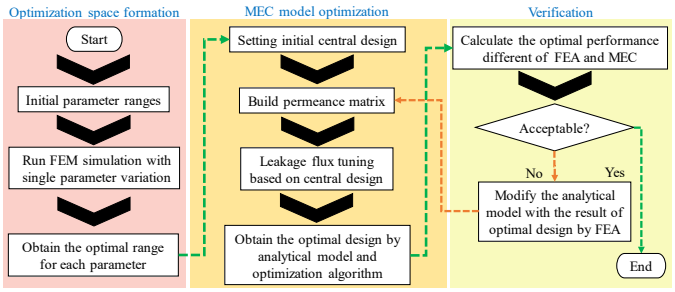

Fig. 13. Hierarchical optimization flow chart.

Specifically, the single-variable FEM simulation is conducted, and the optimal range of each parameter should be obtained. In such case, the effectiveness of the MEC model is ensured.

Afterwards, the simulation results of the central design in the optimization space (i.e., whose geometry parameters are the means of the corresponding optimal range) are set as the paradigm for the leakage flux tuning process in MEC model. Then, with the tuned MEC model and optimization algorithms, the initial optimal design can be obtained.

Later, the electromagnetic performance of the initial optimal design is simulated by FEM, and the stimulated results are compared with that by the MEC model. If the difference exceeds the tolerant value, a new MEC model whose leakage flux tuning is based on the initial optimal design is built, and another round of optimization is conducted. This process is iterated until the difference of the optimal performance by the MEC model and FEM is acceptable.

V. Experimental Verification

To verify the performance of the optimal design generated by the MEC model, a prototype with test bench is manufactured as shown in Fig. 14. Since the working flux flows in radial and axial direction, the circumferential laminated silicon steel is used for both stator module and mover. Three stator modules are arranged with 120 electric degrees interval in both axial and circumferential directions. To individually test the performance under rotary and linear motions, the corresponding servo systems, position encoder, and force/torque meter are set at two terminals of the output shaft. In the machine drive test rig, an XCUBE control board with a dual-core chip as MCU, sensor board and SiC inverters are adopted in monitoring and controlling two sets of three-phase current.

In Fig. 15, the measured coil back-EMF waveforms are illustrated. Coil_1 and Coil_2 are two coils in the same stator module, which share the identical magnitudes of coil back-EMFs under both linear and rotary motions (i.e., 1.51V and 40.85V, respectively). In addition, the back-EMF waveforms of those two coils are in the same phase under linear motion, but complementary to each other under rotary motion. This feature complies with the coil flux linkage waveforms in Fig. 11. With proper mechanical shifting among stator modules, the three-phase systems are formed for both motions. Nonetheless, the unbalanced magnitude issue exits in the three-phase back-EMFs. One of the major reasons is that the physical axial distance between two stator modules is not enough to guarantee the magnetic isolation, which leads to the magnetic interaction between stator modules and end-effect.

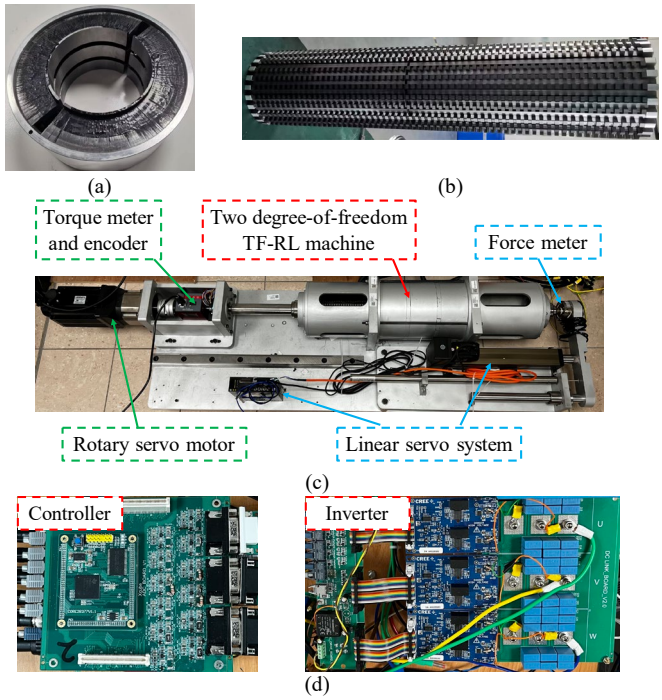

Fig. 14. Experimental setup. (a) Stator module. (b) Mover. (c) The TF-RL machine with test bench. (d) Power drive and control system.

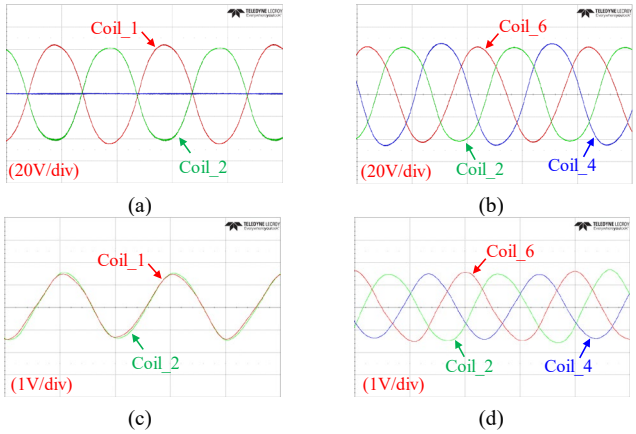

Fig. 15. Measured coil back-EMF waveforms (a) Single module under rotary motion. (b) Three-phase under rotary motion. (c) Single module under linear motion. (d) Three-phase under linear motion.

As to the on-load condition, the saturation effect in the iron part becomes severe under heavy load, resulting in deteriorated rotary torque and linear force. Hence, the no-load back-EMF cannot be utilized directly.

In the MEC model, the magnetic fields generated by PMs and armature current can be obtained at the same time. Hence, the on-load terminal voltage in each coil and the actual power factor can be calculated. According to the diagram of voltage vectors. The saturated back-EMF is acquired and utilized in calculating the linear force and rotary torque. The on-load performance versus current by MEC model, MMF model, FEM and experiments are presented in Fig. 16. Since the saturation effect gets worse with heavier load applied, the amplitude of such saturated back-EMF

would be lower than that of no-load back-EMF. Consequently, the degradation of rotary torque, linear force and power factors of two motions gets severe as heavy load is applied. It also explains why the MEC model is better than the MMF model as the later one utilizes the constant no-load back-EMF for calculating the on-load performance lacking the consideration for the saturation effect.

The measured, calculated, and simulated rotary torque and linear force versus current are presented in Fig. 16. It is noted that the linear force and rotary torque obtained by the MMF model are linear to the current due to lack of consideration on saturation effect. As to the MEC model, the calculated performance is close to that by simulation due to the evaluation on the saturation effects under various load condition.

At light-load region, the force and torque obtained by MEC model and FEM are close. However, at heavy-load region, the saturation effect is more severe in FEM and physical test. Since the permeance grid in the MEC model is much coarser than the mesh grid in FEM, the partial saturation cannot be precisely evaluated in the MEC model, especially when the load keeps increasing. Still, the performances calculated by the MEC model complies well to those by simulation and measurement.

Finally, the major electromagnetic performance of the TF-RL machine, and calculation time of the MMF model, MEC model and FEM are presented in Table III and Table IV. It should be mentioned the coil inductance largely depends on the assembled structure of the TF-RL machine, rather than only the consideration on airgap permeances. Hence, the power factors of two motions by MMF models are not listed.

The measured rated linear force is 377.61N, which is 9.99%, 28.07%, and 5.15% and lower than that by MEC, MMF and FEM, respectively. Besides, the measured rated rotary torque is 32.77 Nm, which is 9.2%, 16.91% and 3.19% lower than that by MEC, MMF and FEM, respectively. Due to the extra resistance brought by the leading copper wire, the power factors under two motions by measurement is slightly higher than those by MEC and FEM.

Apart from the electromagnetic performance, the calculation times of MEC and MMF models are 0.43% and 0.21% of the that by FEM in linear study, and 0.31% and 0.16% in rotary study, respectively. While the MEC model exhibits higher calculation time compared with MMF model, its superior on competitive accurate calculation makes it a highly potential optimization method for 3D model TF-RL machine.

VI. Conclusion

In this paper, a magnetic equivalent circuit model for calculating the performance of a 2DOF TF-RL machine is proposed. In this MEC model, the permeance grid is formed based on the magnetic field pattern plotted by FEM. With the leakage flux tuning, the MEC model is able to calculate the electromagnetic performance of the TF-RL machine under no-load and on-load condition in a high level of accuracy, while the calculation time consumption is about 0.4% of that by FEM. With the fixed model parameters, the MEC model exhibits competitive alignment with FEM under various geometry designs. Hence, it is utilized in a hierarchical optimization flow chart for significantly enhancing the time-efficiency in 3D model optimization. Finally, to verify the effectiveness the MEC model, a prototype is manufactured and tested.

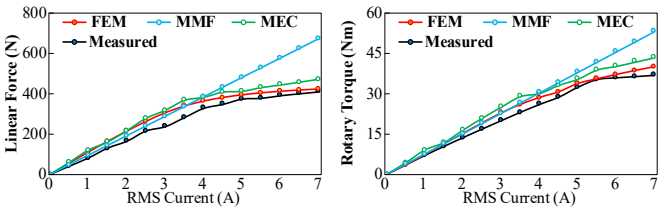

(a) (b)

Fig. 16. The comparison of on-load performances versus load by four methods. (a) Linear force. (b) Rotary torque.

TABLE III
MAJOR PERFORMANCE OF LINEAR MOTION

Method	Force (N)	Power factor	Calculation time (s)	Error (Force)
Experiment	377.61	0.23		
MMF	483.59		3.21	28.07%
FEM	397.04	0.22	1523	5.15%
Proposed MEC	415.33	0.20	6.61	9.99%

TABLE IV
MAJOR PERFORMANCE OF ROTARY MOTION

Method	Torque (Nm)	Power factor	Calculation time (s)	Error (Force)
Experiment	32.77	0.26		
MMF	38.31		4.56	16.91%
FEM	33.97	0.25	2798	3.19%
Proposed MEC	35.78	0.23	8.68	9.20%

References

[1] L. Xie, J. Si, Y. Hu and Z. Wang, "Overview of 2-Degree-of-Freedom Rotary-Linear Motors Focusing on Coupling Effect," *IEEE Trans. Magn.*, vol. 55, no. 4, pp. 1-11, April 2019.

[2] L. Szabó, "On the use of rotary-linear generators in floating hybrid wind and wave energy conversion systems," in *Proc. 2018 IEEE Int. Conf. Automat. Qual. Testing. Robot. (AQTR)*, Cluj-Napoca, Romania, 2018.

[3] L. Szabó, "A Survey on Rotary-Linear Motors Used in Emerging Applications," in *Proc. 45th Annu. Conf. IEEE Ind. Electron. Soc. (IECON)*, Lisbon, Portugal, 2019.

[4] Y. He, S. Cai, Y. Zhou and C. H. T. Lee, "Comparative Study of Two Degree-of-Freedom Rotary-Linear Machines With Permanent-Magnet Mover for High Dynamic Performance," *IEEE Access*, vol. 10, 2022.

[5] G. Jiang, H. Zhou, W. Tao and G. Liu, "Design and Analysis of a Linear-Rotary Fault-Tolerant Consequent-Pole PM Actuator," in *Proc. 13th Int. Symp. Linear Drives Ind. Appl. (LDIA)*, Wuhan, China, 2021.

[6] K. Guo and Y. Guo, "Design and Analysis of a Linear Rotary Permanent Magnet Machine with E-Type Stator Structure," in *Proc. IEEE Int. Conf. Appl. Supercond. Electromagn. Devices (ASEMD)*, Tianjin, China, 2020,.

[7] S. M. Mirić, R. V. Giuffrida, D. Bortis and J. W. Kolar, "Enhanced Complex Space Vector Modeling and Control System Design of Multiphase Magnetically Levitated Rotary–Linear Machines," *IEEE J. Emerg. Sel. Topics Power Electron.*, vol. 8, June 2020.

[8] P. Jin, H. Lin, S. Fang, Y. Yuan, Y. Guo and Z. Jia, "3-D Analytical Linear Force and Rotary Torque Analysis of Linear and Rotary Permanent Magnet Actuator," *IEEE Trans. Magn.*, vol. 49, July 2013.

[9] Y. He, J. Chen, Y. Zhou, L. Cao and C. H. T. Lee, "A Two Degree-of-Freedom Rotary-Linear Machine with Transverse-Flux Structure," *IEEE Trans. Ind. Electron.*, vol. 71, no. 1, pp. 215-225, Jan. 2024.

[10] G. Liu, L. Ding, W. Zhao, Q. Chen and S. Jiang, "Nonlinear Equivalent Magnetic Network of a Linear Permanent Magnet Vernier Machine With End Effect Consideration," *IEEE Trans. Magn.*, vol. 54,Jan. 2018.

[11] R. Alipour-Sarabi, Z. Nasiri-Gheidari and H. Oraee, "Development of a Three-Dimensional Magnetic Equivalent Circuit Model for Axial Flux Machines," *IEEE Trans. Ind. Electron.*, vol. 67, July 2020.

[12] F. Chai, L. Gan and Y. Yu, "Magnetic Field Analysis of an Iron-Cored Tiered Type Permanent Magnet Spherical Motor Using Modified Dynamic Reluctance Mesh Method," *IEEE Trans. Ind. Electron.*, vol. 67, no. 8, pp. 6742-6751, Aug. 2020.

[13] Z. Song and C. Liu, "Energy efficient design and implementation of electric machines in air transport propulsion system," *Applied Energy*, vol. 322, p. 119472, Sep. 2022.

[14] Z. Song, R. Huang, W. Wang, S. Liu and C. Liu, "An Improved Dual Iterative Transient Thermal Network Model for PMSM With Natural Air Cooling," *IEEE Trans. Energy Convers.*, vol. 37, no. 4, pp. 2588-2600, Dec. 2022.

[15] Z. Song and C. Liu, "Electric Machine Design by a Novel Fast Model Predictive Optimization Strategy Treating Dimension-Expensive Problem," *IEEE Trans. Transp. Electrific.*, vol. 9, no. 2, pp. 2683-2692, June 2023.

[16] B. Kou, J. Luo, X. Yang and L. Zhang, "Modeling and Analysis of a Novel Transverse-Flux Flux-Reversal Linear Motor for Long-Stroke Application," *IEEE Trans. Ind. Electron.*, vol. 63, no. 10, pp. 6238-6248, Oct. 2016.

[17] D. Dong, W. Huang, F. Bu and Q. Wang, "Modeling and Optimization of a Tubular Permanent Magnet Linear Motor Using Transverse-Flux Flux-Reversal Topology," *IEEE Trans. Ind. Appl.*, vol. 55, no. 2, pp. 1382-1391, March-April 2019.

[18] X. Zhao and S. Niu, "Development of a Novel Transverse Flux Tubular Linear Machine With Parallel and Complementary PM Magnetic Circuit for Precision Industrial Processing," *IEEE Trans. Ind. Electron.*, vol. 66, no. 6, pp. 4945-4955, June 2019.

[19] J. Luo, B. Kou, X. Yang, H. Zhang and L. Zhang, "Development, Design, and Analysis of a Dual-Consequent-Pole Transverse Flux Linear Machine for Direct-Drive Applications," *IEEE Trans. Ind. Electron.*, vol. 68, no. 7, pp. 6097-6108, July 2021.

[20] K. Guo, Y. Guo and S. Fang, "Flux Leakage Analytical Calculation in the E-Shape Stator of Linear Rotary Motor With Interlaced Permanent Magnet Poles," *IEEE Trans. Magn.*, vol. 58, no. 8, pp. 1-6, Aug. 2022.